Bénard-von Kármán vortex street in a confined geometry: wavelength selection by Kelvin-Helmholtz instabilities

Luc Lebon, Chi-Tuong Pham, Paul Boniface, Laurent Limat

Bénard-von Kármán vortex street in a confined geometry: wavelength selection by Kelvin-Helmholtz instabilities.

L. Lebon[1], P. Boniface[1], C.-T. Pham[1,2] and L. Limat[1]

[1] *Matière et Systèmes Complexes, CNRS and Université Paris Cité, UMR 7057, Paris, France*
[2] *Laboratoire Interdisciplinaire des Sciences du Numérique, CNRS and Université Paris-Saclay, UMR 9015, Orsay, France*

PACS 47.20.Ft – Instability of shear flows
PACS 47.32.ck – Vortex streets
PACS 47.20.-k – Flow instabilities

Abstract – We have reconsidered the formation and stability of a vortex street, induced in a rectangular container by a tape moving at high speed on its free surface. In a certain range of tape velocity and of geometrical aspect ratios, the liquid recirculates along the lateral sides of the pool, which induces two shear flows between the tape and these lateral sides, that undergo two coupled Kelvin-Helmholtz instabilities, giving rise to the vortex street. Contrary to the classical situation of a wake, behind an obstacle, the double row remains static which allows one to study its absolute stability in a static framework. In the present paper we have built a model of the two shear flow instabilities that clarifies the wavelength selection problem, inside the stability tongue predicted long ago by Rosenhead, and reduced by steric arguments that we found in a previous paper. In summary, in terms of fig. 1(b) notations, the mean-wavelength favored by Kelvin-Helmholtz instabilities is given by $2b_{\max} \approx \pi c$, while the maximal wavelength predicted by marginal stability is equal to $2b_{c_1} \approx 5.71\, c$. Our available experimental data are in very good agreement with these results and with the resulting phase diagram depicted on fig. 7 .

Introduction : the confined Bénard - von Kármán vortex street. – The Bénard - von Kármán vortex street is a structure that can be widely observed in the wake of an obstacle inside a stationary parallel flow of large enough velocity : it has been investigated by Bénard [1] and modeled by von Kármán [2,3] more than a century ago : in a two-dimensional inviscid flow a vortex street of point vortices are expected to be stable only if the wavelength of the street $2b$ is linked to the width of the street $2a$ by

$$\frac{a}{b} = \frac{1}{\pi}\,\mathrm{argcosh}\left(\sqrt{2}\right) \approx 0.281. \qquad (1)$$

Although this condition is often well satisfied in experiments, the precise nature of this condition is still under discussion [4–7] ; the stability could be of convective nature and the structure intrinsically unstable in its own framework [8].

When the entire flow is confined between two lateral walls, separated by a distance $2c$, the stability condition is deeply modified. In the 30's theoretical works addressed the question of confined point vortices and in particular, Rosenhead [9] established that the stability condition 1 had to be replaced by a continuous stability tongue in the plane $(a/c,b/c)$ of finite extent.

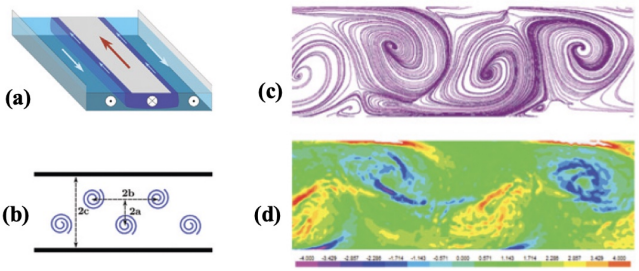

Fig. 1: Experimental study of confined Bénard - von Kármán vortex street (from [10]) : a confined shear flow **(a)** produces a stable vortex street of wavelength $2b$ and width $2a$ **(b)**. **(c)** : typical stream lines of the flow, **(d)** : typical vorticity distribution.

In a previous paper [10], we have presented experiments exhibiting a confined Bénard - von Kármán vortex street by creating a confined shear flow : an endless tape was pulled with a constant speed at the free surface of a water layer in a long pool, of length 2 m, of variable width $2c$ ranging from a few centimeters to 70 cm and of depth h of a few centimeters, see figure 1(a). Because of the mass conservation, a back flow is created in the pool. Under suitable experimental conditions, shear produces a stable vortex street of wavelength $2b$ and width $2a$ as exhibited on figure 1(c) and 1(d). Contrary to the classical situation of a wake, behind an obstacle, the double row remains static which allows one to study its absolute stability in a static framework.

In contrast with the well-known selection rule given by equation 1, we observed that the street system explores a continuous band of stability, consistent with Rosenhead calculations ; we also observed that the experimental points do not cover the whole domain and remain distributed in a rather narrow area. A steric model based on the the finite extent of the vortex cores, not taken into account in the Rosenhead model, can very correctly explain the restriction of the domain explored by the width of the street $2a$. On the other hand, we had no argument to explain the limitation of the domain explored by the wavelengths $2b$ of the streets, particularly the largest ones. In addition, the accumulation of points around mean values remained unexplained too.

In what follows, we propose a model solving these questions. We first remind the classical treatment of this kind of instabilities [11, 12] and then show how to apply this formalism to our particular geometry.

Kelvin Helmholtz instability. – The destabilization of the flow at the origine of the vortex street is here the Kelvin Helmholtz instability: it is the inertial destabilization of sheared layers of fluid [13, 14]. This instability leads to vortices patterns in the flow, with a characteristic length [11, 15, 16] and it appears that these lengths can often be predicted by linear analysis studying the development of a small perturbation at short time. Therefore we will consider here a linear analysis of inviscid parallel shear flows.

Rayleigh Equation for the linearized problem. – We consider a two-dimensional flow since the Squire theorem [17] shows that two-dimensional perturbations are suffisant to find an instability condition for a three-dimensional problem.

In the case of parallel flow along x, the basic velocity field is $\mathbf{V_o}(y) = V_o(y)\,\mathbf{e}_x$ and the pressure field $P_o(y)$. Let's introduce the pertubated fields $\mathbf{v}(x,y,t)$ for the velocity and $p(x,y,t)$ for the pressure.

Let us introduce $\psi(x,y,t)$ the stream function for the pertubated velocity : $v_x = \partial\psi/\partial y$ and $v_y = -\partial\psi/\partial x$.

After linearization, incompressibility and Euler equations lead directly to the following equation :

$$\frac{\partial \Delta\psi}{\partial t} + V_o \frac{\partial \Delta\psi}{\partial x} = V_o'' \frac{\partial \psi}{\partial x} \tag{2}$$

Let us remark that this equation is the transport equation of vorticity without diffusion.

We are searching normal mode solutions of this equation

$$\psi(x,y,t) = \phi(y)\, e^{-i\omega t + ikx} \tag{3}$$

where k is the wave number and ω is the pulsation. Equation 2 leads to the Rayleigh equation :

$$\left(V_o - \frac{w}{k}\right)\left(\phi'' - k^2\phi\right) = V_o''\phi \tag{4}$$

When the flow displays different layers, the normal velocity of the fluid is continuous at the interface between layers while the interface is material. After linearization, this condition leads to the continuity of the ratio $\phi/(V_o - w/k)$ through the interface [18].

We can remark here that, if the basic velocity field V_o is continuous at the interface, then the amplitude of the stream function ϕ is also continuous at the interface.

The flow resolution also needs a stresses expression. In this case, the stress is just the pressure and it can be derived from Euler equation ; let's use $p\,(x,y,t) = \pi(y)\, e^{-i\omega t + ikx}$, and we obtain :

$$\pi = \rho\left(\frac{w}{k} - V_o\right)\phi' + \rho V_o'\phi \tag{5}$$

ρ being the fluid density.

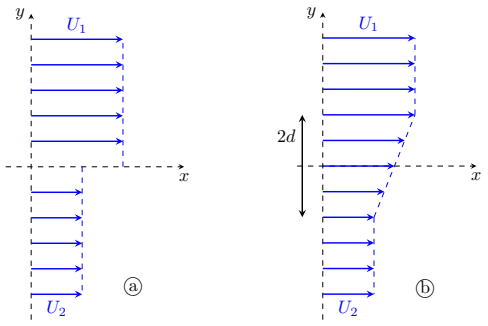

Fig. 2: Simple basic velocity profiles for inviscid shear flow : (a) with velocity discontinuity, (b) with a mixing layer of thickness $2d$.

Shear flow with a velocity discontinuity. – The most basic case is the parallel flow of two fluid layers of different velocities represented on figure 2(a), with a shear of $\Delta U = U_1 - U_2$; at the interface ($y = 0$) the velocity is not continuous.

The dispersion relation of the perturbation velocity field is [18] :

$$\omega = \pm ik\frac{\Delta U}{2} \tag{6}$$

As long as this flow is sheared ($\Delta U \neq 0$), the perturbation growth rate $\sigma = -i\omega$ has a positive solution, so that the flow is unstable. There is no wavelength selection since the smaller the disturbance, the more it is amplified.

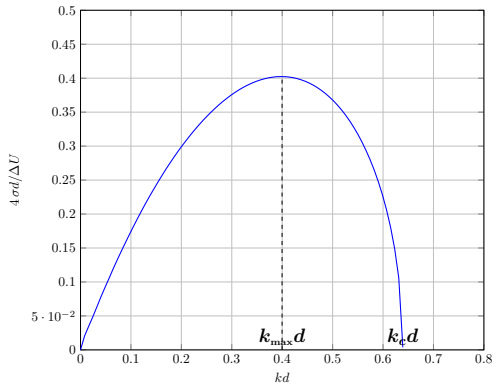

Fig. 3: Dispersion relation for Rayleigh model : an inviscid shear flow with a mixing layer of thickness $2d$ (flow profil of figure 2(b)).

Shear flow with a mixing layer. – In practice, a velocity discontinuity can not persist because of the velocity diffusion induced by viscosity at small scale. Rayleigh introduced a more realistic model with a continuous and piecewise linear velocity field (see figure 2(b)). The thickness of the mixing zone is $2d$. While we consider flows dominated by inertial effects, we assume that d stays constant during the destabilization mechanism.

In this case the dispersion relation becomes [18] :

$$\omega^2 = \left(\frac{\Delta U}{4d}\right)^2 \left[(2kd-1)^2 - e^{-4kd}\right] \tag{7}$$

As soon as $\left[(2kd-1)^2 - e^{-4kd}\right] > 0$, w is real and the perturbation does not amplify. This corresponds to short wavelengths when $k > k_c$ where k_c is the marginal stability wave number. It corresponds to $(2k_c d-1)^2 - e^{-4k_c d} = 0$, *i.e.* $k_c d \approx 0.64$. This result is consistant with the existence of a mixing layer where viscosity effects will stabilize small scale perturbation.

When $k \in [0\,; k_c]$, w is pure imaginary. The growth rate of the instability $\sigma = -i\omega$ is positive and the flow is unstable :

$$\sigma = \frac{\Delta U}{4d}\sqrt{e^{-4kd} - (2kd-1)^2} \tag{8}$$

This dispersion relation is plotted on figure 3. The maximum growth rate is achieved when $k_{\max} d \approx 0.4$, corresponding to a wavelength selection

$$\lambda_{\max} \approx 15.7\, d \tag{9}$$

The size of the mixing zone will select the characteristic wavelength of the instability.

Some works investigated the linear stability of more realistic mixing layer, with smother profiles [19]. First Carrier studied analytically a more complex piecewise linear profile (with 5 domains instead of 3 for the Rayleigh profile) ; he also studied numerically the case of a perfectly smooth profile, very close to the one expected in a real laminar boundary layer between two streams. In both cases he obtained a dispersion relation slightly different from that of the Rayleigh model [20] ; the size of the unstable domain is still $k_c \sim 1/d$ and the most unstable mode $k_{\max} \sim k_c/2$. Physically, we obtain the same behavior whatever the detailed profile of the mixing layer : it stabilizes the wavelengths smaller than its size, and this later select the most amplified wavelength.

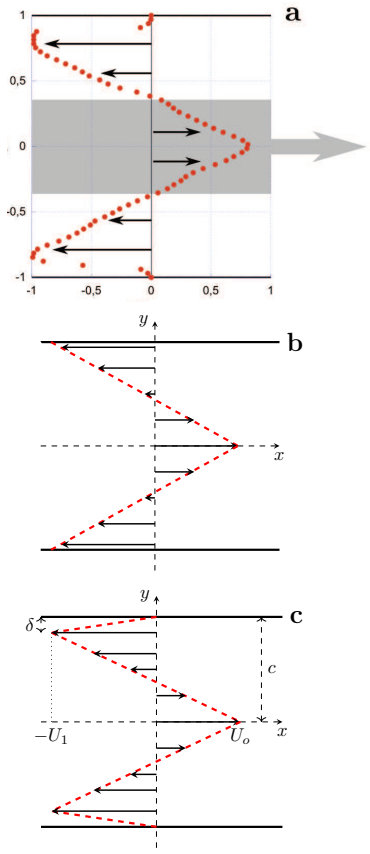

Fig. 4: (a) Basic velocity profil deduced from our confined vortex streets experiments. (b) Piecewise linear model without boundary layer. (c) Piecewise linear model with a boundary layer of thickness δ.

Confined shear flow. – We consider now the confined flow described in the first part exhibiting vortex streets ; a mean flow profil experimentally obtained is represented on figure 4 (a) : a main flow in the center and a back flow on each side.

The simplest basic flow that can approximate this experimental result is a piecewise linear profile without boundary layer as represented on figure 4 (b). However Rayleigh [12] established that the destabilization will occur only if the velocity profile presents at least an inflection point. Therefore we modelize the basic velocity profil including boundary layers as represented on figure 4 (c).

At the center, the fluid flows at a maximum velocity U_o. On each side, the maximum velocity of the back flow U_1 occurs at a distance δ from the wall ; δ is the thickness of

the boundary layer and the velocity is zero on the walls ($y = \pm c$). The mass conservation in the flow leads to :

$$U_1 = U_o \left(1 - \frac{\delta}{c}\right) \tag{10}$$

The basic flow is therefore a piecewise linear flow over four domains:

i	interval	$V_0(y)$	$V_0'(y)$
1	$y \in [c-\delta\ ; c]$	$\frac{U_1}{\delta}(y-c)$	$\frac{U_1}{\delta}$
2	$y \in [0\ ; c-\delta]$	$-\frac{U_0+U_1}{c-\delta}y + U_0$	$-\frac{U_0+U_1}{c-\delta}$
3	$y \in [-c+\delta\ ; 0]$	$\frac{U_0+U_1}{c-\delta}y + U_0$	$\frac{U_0+U_1}{c-\delta}$
4	$y \in [-c\ ; \delta - c + \delta]$	$-\frac{U_1}{\delta}(y+c)$	$\frac{U_1}{\delta}$

In each of them, the Rayleigh equation 4 is solved by $\phi_i(y) = A_i e^{ky} + B_i e^{-ky}$, $(i = 1...4)$. We have five kinematic boundary conditions : the normal velocity v_y is zero on the wall ; while $v_y = -\partial\psi/\partial x = -ik\phi(y)e^{-i\omega t + ikx}$, we obtain $\phi_1(c) = \phi_4(-c) = 0$:

$$A_1 + \alpha B_1 = 0 \tag{11}$$

where $\alpha = e^{-2kc}$, and

$$\alpha A_4 + B_4 = 0 \tag{12}$$

As pointed out previously, the continuity of the basic flow $V_o(y)$ at the boundary of each domain leads to the continuity of $\phi(y)$: therefore $\phi_1(c-\delta) = \phi_2(c-\delta)$, $\phi_2(0) = \phi_3(0)$ and $\phi_3(-c+\delta) = \phi_4(-c+\delta)$ leading to the following relations :

$$A_1 + \beta B_1 - A_2 - \beta B_2 = 0 \tag{13}$$

where $\beta = e^{-2k(c-\delta)}$,

$$A_2 + B_2 - A_3 - B_3 = 0 \tag{14}$$

and

$$\beta A_3 + B_3 - \beta A_4 - B_4 = 0 \tag{15}$$

The stresses (reduced to the pressure in our problem) are also continuous at the boundary of each domain, which leads to tree dynamic boundary conditions : $\pi_1(c-\delta) = \pi_2(c-\delta)$, $\pi_2(0) = \pi_3(0)$ and $\pi_3(-c+\delta) = \pi_4(-c+\delta)$ leading to the following relations :

$$\begin{aligned} &(\omega + k\,U_1 + U_1/\delta)A_1 \\ &+\beta\,(-\omega - k\,U_1 + U_1/\delta)B_1 \\ &-[\omega - k\,U_1 + (U_1+U_o)/(c-\delta)]A_2 \\ &+\beta\,[\omega + k\,U_1 + (U_1+U_o)/(c-\delta)]B_2 \quad = 0 \end{aligned} \tag{16}$$

$$\begin{aligned} &[\omega - k\,U_o - (U_1+U_o)/(c-\delta)]A_2 \\ &+[-\omega + k\,U_o - (U_1+U_o)/(c-\delta)]B_2 \\ &-[\omega - k\,U_1 + (U_1+U_o)/(c-\delta)]A_3 \\ &+[\omega - k\,U_o - (U_1+U_o)/(c-\delta)]B_3 \quad = 0 \end{aligned} \tag{17}$$

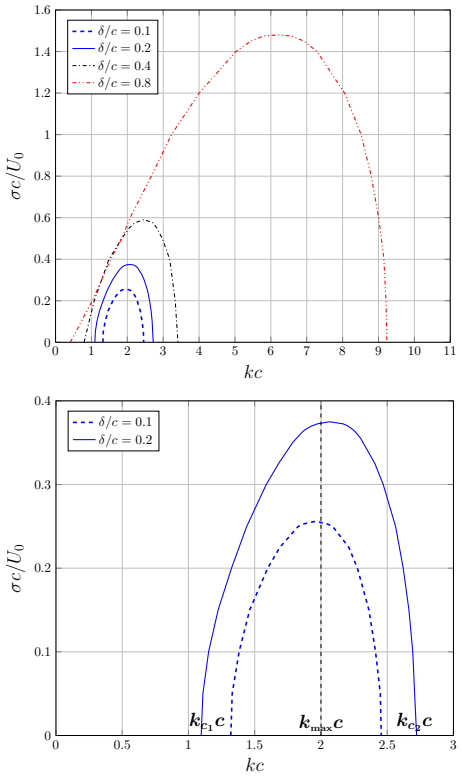

Fig. 5: Dispersion relation for the confined shear flow for different values of the dimensionless thickness of the boundary layer δ/c (flow profil of figure 4(c)).

$$\begin{aligned} &\beta\,[\omega + k\,U_1 + (U_1+U_o)/(c-\delta)]A_3 \\ &+[-\omega - k\,U_1 + (U_1+U_o)/(c-\delta)]B_3 \\ &+\beta\,[-\omega - k\,U_1 + U_1/\delta]A_4 \\ &+[\omega + k\,U_1 + U_1/\delta]B_4 \quad = 0 \end{aligned} \tag{18}$$

Equations 11 to 18 form a system of eight linear homogeneous equations with eight unknowns ; the corresponding system matrix A can be found in Appendix A.

The non trivial solution of this system is obtained when the determinant of the system $\det(A) = 0$; this equation was numerically resolved and we present on figure 5 the dispersion relation for the confined shear flow for different values of the dimensionless thickness of the boundary layer δ/c.

In our experiments, we observe typical value of δ/c between 0.1 and 0.2 (see figure 4(a)). For such thicknesses, the dispersion relation presents a maximum growth rate at $k_{\max}c \approx 2$. The corresponding wavelength $\lambda_{\max} = 2b$ is therefore related to c by

$$\frac{2b}{c} \approx \pi \tag{19}$$

In the case of a shear flow with a mixing, we saw that the most unstable wavelength is controlled by the thickness of the mixing layer d (eq. 9). For a confined shear flow, this wavelength is controlled by the size of confinement $2c$.

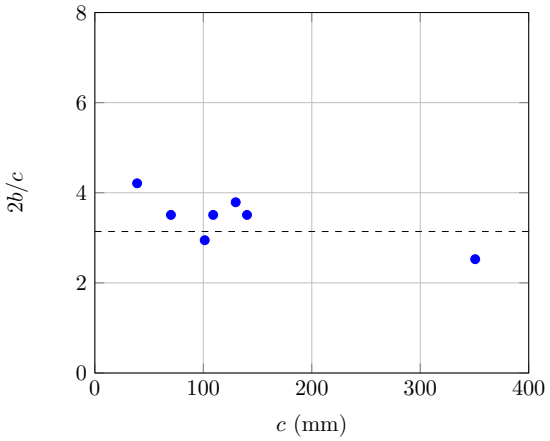

Fig. 6: Dimensionless selected wavelength $\lambda^*_{\max} = 2b/c$: the mean experimental wavelengths (•) are in good agrement with the wavelength predicted by the linear analysis $\lambda^*_{\max} = \pi$ (- -).

This theoretical prediction can be compared to our experiments. On figure 6, we plotted $2b/c$, the selected mean wavelength, measured for different values of the degree of confinement c ; they are in good agreement with the predicted value of π.

The two relevant parameters of this model are the boundary layer thickness δ and the width of the water tank $2c$. This is consistent with our experiments where the water height or the fluid velocity U_o have no influence on observed wavelength.

We plotted the mean experimental wavelength on figure 6 because the measured values are very dispersed around the mean value for a given confinement as plotted on figure 4 of our previous paper [10] ; the origin of such a dispersion is unclear : the flow could be partially turbulent and particularly it is very difficult experimentally to avoid vertical beating of the tape, inducing fluctuations on the flow.

Nevertheless the dispersion relation plotted on figure 5 allows us to predict the marginal stability of the flow, corresponding to the points where the instability growth rate is zero. For example, if $\delta/c = 0.2$, the growth rate is positive for wavenumber between k_{c_1} and k_{c_2} where $k_{c_1}c \approx 1.10$ and $k_{c_2}c \approx 2.72$. As mentioned, in ours experiments we observe typical values of δ/c between 0.1 and 0.2, so that $[k_{c_1}, k_{c_2}]$ corresponds the the largest wavenumber domain where the growth rate is positive. The corresponding wavelengths and positions in the $(\pi a/2c, \pi b/2c)$ plane are :

$$\begin{array}{lll} k_{c_1}c \approx 1.10 & \lambda_{c_1} \approx 5.71\ c & \pi b_{c_1}/2c \approx 4,48 \\ k_{\max}c \approx 2.00 & \lambda_{\max} \approx 3.14\ c & \pi b_{\max}/2c \approx 2.46 \\ k_{c_2}c \approx 2.72 & \lambda_{c_2} \approx 2.31\ c & \pi b_{c_2}/2c \approx 1.81 \end{array} \quad (20)$$

These values and boundaries predicted by the linear analysis can be compared to our experiments : in the $(\pi a/2c, \pi b/2c)$ plane, we plotted all our experimental data on figure 7. As previously pointed out [10], data satisfy the stability area predicted by Rosenhead and steric limitations induced by the rigid disk model. We can observe now that the experimental data points are included between the marginal stability values k_{c_1} and k_{c_2}, where the growth rate of the instability is positive, and as saw on figure 6, the value corresponding to the maximum growth rate passes through the middle of the experimental measurement set.

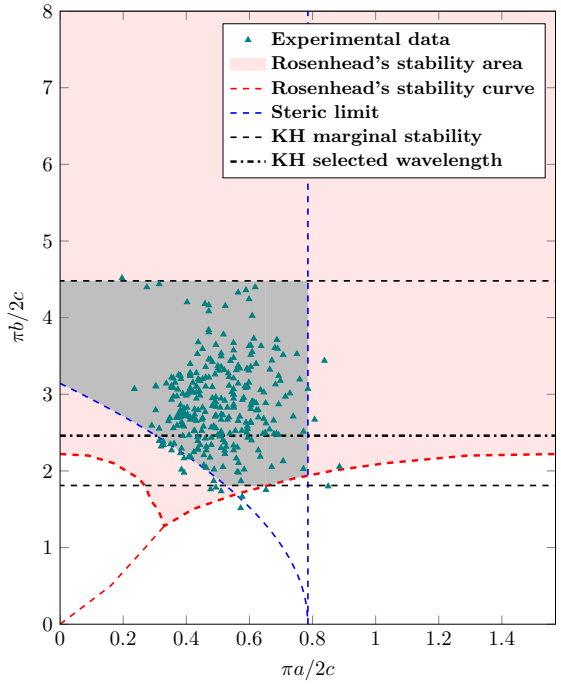

Fig. 7: Stabilty diagram : experimental data compared with theoretical prediction : stability area predicted by Rosenhead, steric limit induced by the rigid disc model and limit induced by Kelvin-Helmholtz marginal stability. The experimental data set satisfy the stability area ( ) predicted by Rosenhead inside the steric and Kelvin Helmholtz marginal stability limitations.

Conclusion. – In summary, we reconsidered the formation of a double Bénard-von Kármán row of vortices, induced in a pool of finite width $2c$ by a tape running at constant speed on its free surface. As expected by this kind of flow, Kelvin-Helmhotz instability leads to a typical wavelength triggered by the sole c, but the possible values observed are dispersed in a continuous domain limited by three effects : (1) this Kelvin-Helmhotz mechanism, (2) the stability of vortex points calculated by Rosenhead, (3) a possible effect due to the finite size of the vortex cores. We have thus ran for the first time a complete description of these phenomena. It would be now interesting to study more complex arrangements of vortices, such as these encountered behind swimming bodies [21, 22] with for instance four rows and possible inversions of the rotation in each row. Also the case of a single vortex row

could be studied, its mechanisms of destabilization remain disputed [23].

Appendix A. – Equations 11 to 18 form a system of eight homogeneous linear equations with eight unknowns ; we present here all the non-zero coefficients of corresponding matrix A used to find numerically the dispersion relation. The coefficients were adimensionalized using as time scale c/U_0 and U_1 was directly derived from U_0 and δ/c from equation 10. Let us remind that $\alpha = e^{-2kc}$ and $\beta = e^{-2k(c-\delta)}$.

$$\begin{array}{ll} a_{11} = 1 & a_{27} = \alpha \\ a_{12} = \alpha & a_{28} = 1 \end{array}$$

$$\begin{array}{ll} a_{33} = 1 & a_{35} = -1 \\ a_{34} = 1 & a_{36} = -1 \end{array}$$

$$\begin{array}{ll} a_{41} = 1 & a_{43} = -1 \\ a_{42} = \beta & a_{44} = -\beta \end{array}$$

$$\begin{array}{ll} a_{55} = \beta & a_{57} = -\beta \\ a_{56} = 1 & a_{58} = -1 \end{array}$$

$$\begin{aligned} a_{61} &= \omega c/U_0 + kc\,(1-\delta/c) + (1-\delta/c)/(\delta/c) \\ a_{62} &= \beta\,[-\omega c/U_0 - kc\,(1-\delta/c) + (1-\delta/c)/(\delta/c)] \\ a_{63} &= -\omega c/U_0 - kc\,(1-\delta/c) + (2-\delta/c)/(1-\delta/c) \\ a_{64} &= \beta\,[\omega c/U_0 + kc\,(1-\delta/c) + (2-\delta/c)/(1-\delta/c)] \end{aligned}$$

$$\begin{aligned} a_{73} &= \omega c/U_0 - kc - (2-\delta/c)/(1-\delta/c) \\ a_{74} &= -\omega c/U_0 + kc - (2-\delta/c)/(1-\delta/c) \\ a_{75} &= -\omega c/U_0 + kc - (2-\delta/c)/(1-\delta/c) \\ a_{76} &= \omega c/U_0 - kc - (2-\delta/c)/(1-\delta/c) \end{aligned}$$

$$\begin{aligned} a_{85} &= \beta\,[\omega c/U_0 + kc\,(1-\delta/c) + (2-\delta/c)/(1-\delta/c)] \\ a_{86} &= -\omega c/U_0 - kc\,(1-\delta/c) + (2-\delta/c)/(1-\delta/c) \\ a_{87} &= \beta\,[-\omega c/U_0 - kc\,(1-\delta/c) + (1-\delta/c)/(\delta/c)] \\ a_{88} &= \omega c/U_0 + kc\,(1-\delta/c) + (1-\delta/c)/(\delta/c) \end{aligned}$$

* * *

We are indebted to stimulating discussions with C. Arratia and J. E. Wesfreid around instability mechanisms.

REFERENCES

[1] Bénard H., *Comptes Rendus de l'Académie des Sciences*, **147** (1908) 970.
[2] von Karman T., *Nachrichten von der Gesellschaft der Wissenschaften zu Göttingen, Mathematisch-Physikalische Klasse*, (1911) 509.
[3] von Karman T. and Rubach H., *Phys. Z*, **13** (1912) 49.
[4] Saffman P. and Schatzman J., *J. Fluid Mech.*, **117** (1982) 171.
[5] Kida S., *J. Fluid Mech.*, **122** (1982) 487.
[6] Meiron D., Saffman P. and Schatzman J., *J. Fluid Mech.*, **147** (1984) 187.
[7] Jimenez J., *J. Fluid Mech.*, **178** (1987) 177.
[8] Mowlavi S., Arratia C. and Gallaire F., *Journal of Fluid Mechanics*, **795** (2016) 187.
[9] Rosenhead L., *Philos. Trans. Roy. Soc. London*, **228** (1929) 275.
[10] Boniface P., Lebon L., Limat L. and Receveur M., *Europhysics Letters*, **117** (2017) 34001.
[11] Drazin P. and Reid W., *Hydrodynamic stability* (Cambridge university press) 2004.
[12] Rayleigh L., *Proc. Lon. Math. Soc.*, **10** (1880) 57.
[13] von Helmholtz H., *Philos. Mag.*, **36** (1868) 337.
[14] Kelvin L., *Philos. Mag.*, **42** (1871) 362.
[15] Thorpe S., *J. Fluid Mech.*, **39** (1969) 25.
[16] Dyke V., *Album of Fluid motion* (Parabolic Press Stanford) 1982.
[17] Squire H. B., *Proc. R. Soc. Lond. A*, **142** (1933) 621.
[18] Charru F., *Instabilités Hydrodynamiques* (EDP Sciences/CNRS Editions) 2007.
[19] Carrier G., *Los Alamos Internal Report*, (1954) .
[20] Esch R., *J. Fluid Mech.*, **3** (1957) 289.
[21] Stremler M. A., Salmanzadeh A., Basu S. and Williamson C. H., *J. Fluids Struct.*, **27** (2011) 774.
[22] Stremler M. A. and Basu S., *Fluid Dyn. Res.*, **46** (2014) 061410.
[23] Arratia C., Mowlavi S. and Gallaire F., *Phys. Rev. Fluids*, **3** (2018) 053901.